Geomechanical implications of carbon sequestration in carbonate saline aquifer

Haoyue Wang
Advisor: Bradford Hager and Brian Evans

Abstract

The use of satellite-based interferometric synthetic aperture radar (InSAR) to detect subtle ground deformation is a cost-effective monitoring method for geological storage of carbon dioxide. In this paper we performed coupled simulation of two-phase flow and geomechanics to investigate the ground deformation induced by the sequestration of CO_2 into carbonate saline aquifer. For injection in the Nisku carbonate formation in Alberta, Canada, the ground surface is uplifted by a maximum of 2.3 cm at the end of 5 years' injection assuming a poroelastic constitutive law. Previous experimental studies suggest the carbonate rock becomes less rigid and more permeable when its solid matrix is partly dissolved by acidic water. In the scenario of high injection rate and low reservoir permeability, the flow field is dominantly by pore water flowing horizontally away from the injection well. This along with the fact that injected CO_2 is dry suggest the available water in altering rock property is limited to the pore water. Under this closed-system hypothesis, a maximum 2 percent decrease in rock stiffness and a maximum two-fold increase in permeability are estimated. The ground deformation obtained from chemo-mechanical model incorporating such material property changes is close to that from poroelastic simulation in the first five years. However, change in rock permeability is expected to bring in complicated ground deformation when CO_2 is injected at a constant rate and water pressure is maintained hydrostatically at the far field by pumping.

1 Introduction

Global carbon dioxide emissions from fossil-fuel combustion and cement production surpassed 33 Gt of CO_2 in 2010 and are projected to increase [*Peters et al.*, 2011]. Capture and geological storage of CO_2 provide a way to curtain CO_2 emission into the atmosphere, by capturing CO_2 from major stationary sources, transporting it usually by pipeline and injecting it into suitable deep rock formations [*Benson et al.*, 2005]. The abundance of carbonate reservoir with suitable porosity and permeability over the world suggests enormous potential of CO_2 storage in carbonate saline aquifer. However, since acidified aqueous solution can dissolve a lot of carbonate minerals and the reactions are fast, the mechanical and transportation properties of the rock matrix will be altered along the injection. For instance, an injection operation would be halted if the permeability of the saline aquifer decreased significantly over time. Hence, a better understanding of the underlying physics is crucial for successful storage of CO_2 in carbonate formations.

The use of satellite-based interferometric synthetic aperture radar (InSAR) to detect subtle ground deformation is a cost-effective monitoring method for geological storage of carbon dioxide [*Mathieson et al.*, 2010]. This technique has been applied to an industrial-scale CO_2 storage project at In Salah in Algeria. An injected mass of 3 million tons of carbon dioxide via several horizontal wells produces a measurable surface uplift of approximately 5 mm/year [*Vasco et al.*, 2010]. The targeted reservoir in the In Salah project is a sandstone formation, and numeric studies with a poroelastic constitutive law [*Preisig and Prévost*, 2011; *Rutqvist et al.*, 2010] match the magnitude of the observed

uplift. For carbonate saline aquifers, the simple poroelastic constitutive law may no longer apply and the observed ground deformation may be more difficult to interpret.

In this paper we study the chemomechanical interaction between carbonate rock and aqueous solution in equilibrium with high pressure CO_2, and simulate the ground deformation due to carbon sequestration in a carbonate formation in Alberta, Canada with the new constitutive law. In section 2, we present the properties of the CO_2-H_2O-$CaCO_3$ system and their implications for CO_2 sequestration. In section 3, we estimate the impact of CO_2 injection on the mechanical and transportation properties of carbonate rock. Section 4 gives the ground deformation when a poroelastic constitutive law is used. In section 5, we obtain a more realistic result when the material properties discussed in section 3 are used. Section 6 concludes the study.

2 Properties of Brine-CO_2-$CaCO_3$ system

2.1 Chemical and physical properties of brine-CO_2 system

When injected into saline aquifer, CO_2 migrates as part of the non-isothermal two-phase flow of brine and CO_2, and their densities, viscosities, enthalpies and thermal conductivities are the key physical properties governing such flow (Fig. 1). The properties of each phase depend on temperature, pressure, as well as the dissolved amount of the other phase. Under temperature and pressure conditions relevant to saline aquifer injection, the molar fraction of H_2O in CO_2 phase is smaller than 0.025 and molar

fraction of CO_2 in aqueous phase is smaller than 0.05 [*Lu et al.*, 2009]. At least in two cases, such amount of mutual solubility between CO_2 and aqueous phase is important.

One is the altercation of the mobility of CO_2 near the well region due to the solubility of water in CO_2 phase [*Hurter et al.*, 2008]. While the dissolution of irreducible water (shown in the zoomed-in box on the left of Fig. 1) into the CO_2 phase leads to higher relative permeability, the ensuing precipitation of salt reduces the intrinsic permeability. It is in case of pore throat being the deposition site that the later mechanism reduces injectivity dramatically. The net change of the mobility of CO_2 is thus unpredictable and not considered in this study. The other case is the gravity-driven fingering (shown in the zoomed-in box on the right of Fig. 1) arising from the dependence of brine density on the dissolved CO_2, which dictates the long-term transportation of CO_2. For typical aquifers, a dimensional analysis shows that for a permeability variation of 1−3000 mD, the critical time can vary from 2000 years to about 10 days while the critical wavelength can vary between 200m and 0.3m [*Riaz et al.*, 2006]. This suggests the vertical convection of the acidic water quickly sets in for a high permeability formation while the same phenomenon will become important only in the long run for a low permeability formation.

Nordbotten and Celia [*Nordbotten and Celia*, 2006] found in the short term the shape of the injected CO_2 plume depends critically on the non-dimensional parameter that is proportional to the ratio of permeability over injection rate. For the case of relatively high injection rate, the migration of the pore water in the aquifer in the short run is dominantly in the horizontal direction. We focus on such a case (Fig. 1) in this study as the impact of convection due to the gravitational instability from dissolved CO_2 in water

can be safely ignored for the injection in the first ten years. In this scenario, it is the high pressure at the injection well and the density difference between CO_2 phase and brine that drives the two-phase flow. And the limited mutual solubility justifies the replacement of the properties of mixtures by those of brine alone and CO_2 alone as done in many previous studies [*Morris et al.*, 2011; *Preisig and Prévost*, 2011].

2.2 The solubility of the brine-CO_2-$CaCO_3$ system

Among the minerals that compose carbonated rock, calcite is more chemically active than dolomite due to its weaker ionic bonds, and therefore the focus of this study. The solubility of CO_2 is mildly affected by the presence of calcite due to the small calcite solubility. On the other hand, the dissolution of high pressure CO_2 in brine significantly reduces its pH and results in tens of times higher calcite solubility [*Duan and Li*, 2008]. Fig. 2 shows the pH and calcite solubility in the system as a function of CO_2 partial pressure.

In the case described at the end of section 2.1 and Fig. 1, i.e., the CO_2 are injected at a high rate compared to the formation permeability, the water is mainly migrating horizontally away from the injection zone. This along with the fact that injected CO_2 is dry suggests for an arbitrary enclosed space the available volume of water to dissolve the rock in that space is the pore volume in the rock. Under this hypothesis, the maximum calcite solubility of 0.08mol/L in Fig. 2 could be translated into on average 0.3% of the solid matrix being dissolved for a calcite-made carbonate reservoir with 10% porosity. Assuming the heterogeneity of the permeability field is not too pronounced, the average

values above are also the representative values. We refer the situation with limited dissolving water the closed-system hypothesis [*Grgic*, 2011] hereafter in this paper.

3. The mechanism of short-term rock altercation

The injection of carbon dioxide induces changes in stress and pore pressure, and thus produces deformation in rock. Constitutive law that describe the poroelastic behavior of intact rock can be written as:

$$\sigma_{ij} + (bp + K\alpha T)\delta_{ij} = \lambda\varepsilon_{kk}\delta_{ij} + 2\mu\varepsilon_{ij}, \quad (1)$$

where σ_{ij} is the stress tensor (with positive value indicating tensile stress), ε_{ij} is the strain tensor, ε_{kk} is the volumetric strain, μ is the shear modulus, λ is the drained Lame´ constant, K is the drained bulk modulus, α is the volumetric thermal expansion coefficient for the solid, and b is the Biot's coefficient. Biot's coefficient can be measured in lab or indirectly estimated from the compatibility relation as $1 - K / K_s$, where K_s is the bulk modulus of the solid matrix and equals the bulk modulus of the solid grain if no occluded porosity exists [*Coussy*, 2004].

As CO_2 dissolves into brine, the equilibrium between brine and surrounding carbonates breaks and part of the rock matrix would be dissolved. If such dissolution happens under no confining pressure, then the pore volume will increase and as a result the permeability will increase and the rock matrix will become less stiff. Conversely, the ensuing mechanical compaction under confining pressure tends to decrease the pore volume, and thus decrease the permeability and make the rock stiffer.

3.1 Permeability change

Vialle and Vanorio performed permeability tests on carbonate rock samples before and after the injection of water saturated with CO_2 [*Vialle and Vanorio*, 2011]. In their experiments, the pH of the injected fluid is about 3.2, and the Darcy velocity is about 11~23 m/day, which is higher than the values encountered in the field. In one of their experiments, a fivefold increase in permeability is observed when the porosity of the corresponding sample increases from 26.49% to 31.46% after 700 pore volumes of acidic fluid is injected. The measured calcium ion concentration at the outlet is 0.0057 mol/L, which is lower than the values shown in Fig. 2 and suggests the fluid is undersaturated with respect to calcite. However, in the same set of experiments most of the seismic velocity reductions happen in the first 100 pore volumes. We assume the changes in permeability also happen in the first 100 pore volumes to find the maximum possible changes in permeability. In the case that all the dissolving water is the pore water and the maximum solubility of calcite in the aqueous phase is reached (0.08 mol/L; Fig. 2), linear interpolation would result in a maximum two-fold permeability increase under the closed-system hypothesis.

Compared to the time scale of fluid injection, the dissolution of calcite in acidic aqueous solution happens “instantly”. Hence the permeability can be modeled as a two-state function, and the transition from the initial state to the final state happens only after the CO_2 saturation has reached a threshold value, i.e., after the CO_2 plume has swept the rock in concern:

$$k = \begin{cases} k_0, \ S_{\mathrm{nw}} < S_{\mathrm{cri}} \\ k_1, \ S_{\mathrm{nw}} \geq S_{\mathrm{cri}} \end{cases}, \tag{2}$$

where the subscripts 0 and 1 denote the values before and after the altercation by the acidic water, and S_{nw} is the CO_2 saturation. S_{cri} is the critical value that once the CO_2 saturation has reached no further change in rock property by net dissolution of carbonate mineral would happen.

3.2 Stiffness change

In the same set of flow-through experiments, Vialle and Vanorio [2011] observed a decrease of the dry sample P- and S- wave velocities and thus a reduction in the dynamic elastic moduli after carbonate rock samples are flushed by water saturated with high pressure CO_2. There are similar flow-through experiments [*Grgic*, 2011; *Le Guen et al.*, 2007], but it is the axial strain of the cylindrical carbonate rock samples under triaxial load being measured, which becomes more and more negative (negative strain means compressive strain) over the course of each experiment. Based on these experimental observations, we consider a simple constitutive relation:

$$\sigma_{ij} + (\tilde{b}p + \tilde{K}\alpha T)\delta_{ij} = \tilde{\lambda}\varepsilon_{kk}\delta_{ij} + 2\tilde{\mu}\varepsilon_{ij}, \tag{3}$$

where all the static elastic moduli $\tilde{K}$, $\tilde{\lambda}$, $\tilde{\mu}$ and Biot's coefficient $\tilde{b}$ are functions of f, the fraction of solid matrix being dissolved. As in section 3.1, these elastic moduli can be similarly modeled as two-state functions:

$$\tilde{K} = \begin{cases} K_0, S_{\text{nw}} < S_{\text{cri}} \\ K_1, S_{\text{nw}} \geq S_{\text{cri}} \end{cases}, \tilde{\lambda} = \begin{cases} \lambda_0, S_{\text{nw}} < S_{\text{cri}} \\ \lambda_1, S_{\text{nw}} \geq S_{\text{cri}} \end{cases}, \tilde{\mu} = \begin{cases} \mu_0, S_{\text{nw}} < S_{\text{cri}} \\ \mu_1, S_{\text{nw}} \geq S_{\text{cri}} \end{cases}. \quad (4)$$

As the magnitude of the bulk modulus of the solid matrix K_s is typically much larger than the drained bulk modulus K, Biot's coefficient $\tilde{b}$ in Eq. 3, which equals $1 - \tilde{K} / K_s$, is assumed to unchanged over the course of the injection. As there is no direct measurement of the change of the static moduli to our knowledge, it is estimated from the dynamic moduli change measured in Vialle and Vanorio (2011). In their experiment conducted at a confining pressure of 8 MPa (their other experiments with a 1.1 MPa confining pressure is considered too low to be applicable to the field), the carbonate rocks experience a maximum 6% reduction in P-wave velocity and a maximum 11% reduction in S-wave velocity after 100 pore volume of acidic fluid has been injected. We assume uniform reduction for all the elastic moduli, and under closed system hypothesis the data would imply a maximum of a two percent reduction in the elastic moduli, i.e., $K_1 = 0.98K_0,\ \lambda_1 = 0.98\lambda_0,\ \mu_1 = 0.98\mu_0$.

The two percent reduction in elastic moduli estimated in this subsection and the two fold of increase in permeability estimated in subsection 3.1 can bound the maximum possible material property change for the carbonate rocks measured by Vialle and Vanorio [*Vialle and Vanorio*, 2011]. For any other carbonate formation considered for CO_2 injection, the potential changes in permeability and stiffness must be measured in lab. However, we will use the estimates above in the ground deformation simulation in section 5 to assess the geomechanical consequences of these changes in a general sense.

4 Poroelastic simulation of carbon sequestration in saline aquifer

4.1 Carbon sequestration at central Alberta, Canada

There are more than 150 Mt CO_2 emissions from large stationary sources (>100 kt CO_2 per year each) in Alberta, Canada [*Bachu and Bennion*, 2008]. The existence of large stationary sources makes carbon sequestration in the underlain basin particularly attractive. The Wabamun Area CO_2 Sequestration Project (WASP) provides a comprehensive characterization of large-scale CO_2 storage opportunities over 5000-km^2 area in central Alberta [*Lavoie and Keith*, 2010], and thus sufficient geomechanical, geochemical, and geophysical knowledge regarding the targeted Nisku carbonate formation and the overlain and underlain formations exists (Table 1).

When a horizontal well or a line of vertical wells is drilled, the fluid flow and the deformation along the direction of the horizontal well or the line can be ignored in the middle part of well or line, where a 2D-flow and plain-strain model (Fig. 3) is adequate. If the dip of the formation is zero, then only half of domain needs to be simulated. CO_2 is injected in the Nisku formation that spans from a depth of 1860 m to 1930 m (the 5^{th} layer in Fig. 3). The injection well lies at the symmetry plane (Fig. 3) and is 10 m above the reservoir bottom. The two-phase flow is confined within this formation as the capillary entry pressure of the cap rock is more than 70 MPa [*Bachu and Bennion*, 2008]. The size of the perforation is so small that nearby rock has to be artificially fractured to ease the injection of CO_2. In Fig. 3, the 10 m by 10 m square in the reservoir represents this fractured zone and is set with a higher permeability of 1 Darcy.

4.2 Governing equations

Poroelastic simulation of the injection of carbon dioxide in saline aquifer serves as the basis of any modeling with more realistic constitutive relation. The detailed derivation of the governing equations can be found in Coussy (2004). The reservoir and its immediate overburden and underburden are simulated with poroelastic constitutive law, while other part of the domain is modeled with elastic behavior due to the lack of data. The constitutive law of poroelastic material is Eq. 1 and the momentum balance equation is written as

$$\nabla \cdot \sigma + \rho \vec{g} = 0, \tag{5}$$

where $\vec{g}$ is the gravitational acceleration. ρ is the density of the mixture and equals $\rho_s(1-\phi)+\phi(S_{\mathrm{w}}\rho_{\mathrm{w}} + S_{\mathrm{nw}}\rho_{\mathrm{nw}})$, where ϕ is the rock porosity, ρ are the densities, S are the saturations of fluid phases, and the subscripts s, w, and nw denote the solid matrix, the brine and the CO_2 phase respectively. The Darcy velocities of the brine and the CO_2 phase are governed by the multiphase extension of Darcy's law:

$$\vec{u}_{\mathrm{w}} = \frac{kk_{\mathrm{rw}}}{\eta_{\mathrm{w}}}\nabla(p_{\mathrm{w}} + \rho_{\mathrm{w}} gz),\ \vec{u}_{\mathrm{nw}} = \frac{kk_{\mathrm{rnw}}}{\eta_{\mathrm{nw}}}\nabla(p_{\mathrm{nw}} + \rho_{\mathrm{nw}} gz), \tag{6}$$

where k is the absolute permeability of the rock, k_{r} are the relative permeabilities, η are the viscosities, p are the fluid pressures, and z is the vertical coordinate. The difference between CO_2 pressure and brine pressure is the capillary pressure, which is typically assumed to be a function of the CO_2 saturation. The mass balance equations of fluid are

$$\phi\frac{\partial(\rho_{\mathrm{w}}S_{\mathrm{w}})}{\partial t}+\nabla\cdot(\rho_{\mathrm{w}}\vec{u}_{\mathrm{w}})=-\rho_{\mathrm{w}}S_{\mathrm{w}}\frac{\partial\phi}{\partial t},$$
$$\phi\frac{\partial(\rho_{\mathrm{nw}}S_{\mathrm{nw}})}{\partial t}+\nabla\cdot(\rho_{\mathrm{nw}}\vec{u}_{\mathrm{nw}})=-\rho_{\mathrm{nw}}S_{\mathrm{nw}}\frac{\partial\phi}{\partial t}. \quad (7)$$

And the poroelastic evolution of porosity is governed by

$$\frac{\partial\phi}{\partial t}=b\frac{\partial\varepsilon_{kk}}{\partial t}+\frac{1}{N}\frac{\partial p}{\partial t}-\alpha(b-\phi_0)\frac{\partial T}{\partial t}, \quad (8)$$

where ϕ_0 is the starting porosity, and $\frac{1}{N}$ is the inverse of Biot's tangent modulus linking the porosity variation to pressure variation and equals $\frac{b-\phi_0}{K_S}$ by compatibility requirement. Fluid pressure in Eq. 5, 6 and 10 is in general an appropriate interpolation between brine pressure and CO_2 pressure, but is assumed to equal to brine pressure in this study given the capillary pressure is small. The evolution of temperature is governed by the energy conservation equation

$$[(1-\phi)\rho_{\mathrm{s}}C_{\mathrm{s}}+\phi\rho_{\mathrm{f}}C_{\mathrm{f}}]\frac{\partial T}{\partial t}=$$
$$-\rho_{\mathrm{f}}C_{\mathrm{f}}\vec{q}_{\mathrm{f}}\cdot\nabla T+\frac{1}{T}\nabla\cdot[K_T\nabla T]-K\alpha T\frac{\partial\varepsilon_{kk}}{\partial t}+[\alpha(b-\phi_0)+\phi\alpha_{\mathrm{f}}]T\frac{\partial p}{\partial t}, \quad (9)$$

where C_{s} is the specific heat of solid matrix, ρ_{f} is fluid density, C_{f} is the average specific heat of fluid, $\vec{q}_{\mathrm{f}}$ is the average flow velocity of the fluid, α_{f} is the average of the volumetric thermal expansion coefficient of solid and K_T is the average of thermal conductivities of solid, brine and CO_2. Eq. (11) states the change of temperature is the result of convection, thermal diffusion and work done to the system by pressure and mean stress. As the solid is typically much stiffer compared to the CO_2 phase, the temperature effect of solid deformation in Eq. 11 is further ignored.

Taking the brine pressure, the CO_2 saturation, the temperature and the displacements as the primary unknown variables, Eq. 5, 7 and 9 can be solved with supplementary equations, boundary conditions and initial conditions. The mechanical property from [*Goodarzi and Settari*, 2009] and [*Nygaard*, 2010], the transportation property from [*Bennion and Bachu*, 2010] and [*Ghaderi and Leonenko*, 2009], and the thermal property from [*Robertson*, 1988], [*Clauser and Huenges*, 1995] and [*Waples and Waples*, 2004] for each formation are used in this study (Table 1). The properties of brine from [*Batzle and Wang*, 1992], [*Sengers et al.*, 1984] and [*Sun et al.*, 2008] and the properties of CO_2 from [*Span and Wagner*, 1996], [*Fenghour et al.*, 1998] and [*Scalabrin et al.*, 2006] are used.

4.3 Proper boundary and initial conditions

The domains for water flow are the blue and yellow blocks in Fig. 3, and the initial pore pressure is assumed to be hydrostatic. There is no flow at the symmetry plane, and the pressure at the other boundaries is kept at hydrostatic values. The propagation of pressure in the far field is governed by a diffusion-like equation, and the characteristic diffusivity is $\frac{k}{\eta}\frac{1}{\frac{1}{N}+\frac{\phi_0}{K_{\mathrm{w}}}}\frac{K+\frac{4}{3}\mu}{K_u+\frac{4}{3}\mu}$ [*Coussy*, 2004], where K_{w} is the bulk modulus of water and K_u is the bulk modulus of the undrained solid. For formation properties listed in Table 1, water compressibility of 2.8×10^{-10} Pa^{-1} [*Batzle and Wang*, 1992] gives a characteristic length of 13 km after 5 years' injection. Hence the rightmost hydrostatic boundary (Fig. 3) represents the case where water is being artificially pumped out there.

The domain for CO_2 flow is the blue block in Fig. 3. 0.2 Mt/km CO_2 is injected via the left side of the 10m by 10 m square, and CO_2 is not allowed to flow across the other boundaries.

Geomechanics is simulated in the entire domain shown in Fig. 3. The top boundary is traction-free, the right and the bottom boundary have zero normal and tangential displacements, and the left boundary is a symmetry plane. One of the main concerns in building a geomechanical model is to avoid the effects of incorrect boundaries on the solution. Yet the implementation of the ideal boundary condition that there is no displacement and deformation at infinity using finite element method incurs extra computational cost in the uninterested region. In this study, we use infinite element, element defined over semi-infinite domain with suitably chosen decay function, e.g., Zienkiewicz et al., 1983, to reduce the computational cost while preserve the far field boundary conditions. The infinite element calculations are done at the outmost layer at the bottom and the right in Fig. 3.

The injected fluid is 30 degree colder than the reservoir, where initially a 28K/km geothermal gradient exists. The symmetry plane is adiabatic and the other boundaries are fixed at their initial temperature.

4.4 Benchmark the simulation

The simulation is carried out using the COMSOL Multiphysics software package, with which we have performed many successful benchmark tests.

One type of benchmarking problem is the proper coupling between fluid flow and deformation. Fig. 4A shows the problem of sudden pressurization of an infinitely long porous cylinder. The cylinder initially has a constant pore pressure. When a radial traction is applied to the cylinder, the pore pressure immediately increases to the undrained value. Without further flow-deformation coupling, the excess pressure will drain away monotonically with time. Yet, more rapid drainage at the cylinder edge leads to more traction loaded on the solid and for a short period of time the pressure at the center of the cylinder keeps increasing. In Fig. 4B, the expected non-monotonic evolution of pore pressure from the quasi-analytical solution is nicely captured by COMSOL simulation.

The other type of benchmarking problem is the simulation of ground deformation in a half-space. Fig. 5A shows the ground deformation induced by a vertically opened tensile crack [*Okada*, 1985], and Fig. 5B shows the ground deformation induced by a uniformly pressurized spherical cavity [*Mogi*, 1958]. While the results from finite element only simulations in a small domain deviate from the analytical solution, the results from finite/infinite element simulation in the same domain matches the half-space analytic solution very well.

4.5 Results

The duration of the simulation is five years. Fig. 6 shows the CO_2 saturation at the end of each year, and the irreducible water occupies half of the pore volume after the CO_2 plume has passed. The trapped water is highly acidic and is saturated with calcite. Fig. 7 shows

the temperature at the end of year 1, 2, 3 and 5. The small porosity and the low flow speed (the maximum flow speed is about 0.1 m/day at the end of year 5) result in the diffusion-like thermal profile. Fig. 8 shows the evolution of pore pressure in the middle plane of the reservoir. Under high pressure water is highly incompressible, and as a result the pressure propagates much faster than the CO_2 plume (cf. Fig. 6). Fig. 9A shows the thickness of the inflated reservoir, and Fig. 9B shows the vertical displacements at the ground surface. The injected cold CO_2 induces thermal contraction of rock near the injection well, which leads to the local minimum of reservoir thickness in Fig. 9A. In Fig 9B, the surface uplift increases with time yet the increment decreases with time. This is in accord with the pressure evolution in Fig. 8. At the injector (Fig. 3) CO_2 is injected at a constant rate while on the right boundary water pressure is artificially kept at the initial pressure (by pumping water out; Fig. 3). For sufficiently long time, a quasi-steady pressure gradient would be established. Since the pore pressure change is the dominant cause of surface uplift, a quasi-steady ground deformation would be attained as well.

5 Chemo-mechanical simulation of carbon sequestration in saline aquifer

As discussed in section 3, the injection of high pressure CO_2 into saline carbonate aquifer can potentially lead to change in rock permeability and stiffness. In addition, if the extent of mechanical compaction is small compared to chemical dissolution, the porosity of the rock matrix will increase as well, which is experimentally observed [*Vialle and Vanorio*, 2011]. Under the closed-system hypothesis, we estimate an increase of the porosity by

0.003 due to mineral dissolution for the reservoir rock in Table 1. We test the effect of the estimated 2-fold change in permeability, 2 percent decrease of the rock stiffness, and 0.003 increase in porosity on the ground deformation. Especially, the effect of stiffness change can be incorporated in the following way:

$$\frac{\partial}{\partial x_j}[\tilde{\lambda}\varepsilon_{kk}\delta_{ij} + 2\tilde{\mu}\varepsilon_{ij}] - b\frac{\partial \Delta p}{\partial x_i} - \alpha K^0 \frac{\partial \Delta T}{\partial x_i} + \Delta f_i + (1-\beta)(f_i^0 - b\frac{\partial p^0}{\partial x_j}) = 0, \quad (10)$$

which is the combination of constitutive law and the momentum balance equation. The first term being differentiated is the effective stress to be solved, where the strain ε_{ij} is zero before the injection. Δp and ΔT are the changes of pore pressure and temperature, respectively, and their derivative can be treated as body forces in Eq. 10. Δf_i is the change in body force due to the density change. β is a binary variable that takes the value of 0.98 when the CO_2 saturation S_{nw} is no less than the critical value S_{cri} (which is assigned to 0.1) and the value of 1 otherwise. The last term in Eq. 10 as a whole represents the impact of the initial stress before the injection when the rock stiffness changes. Using Eq. 2, 3, 10 and the equations in the subsection 4.2, we can calculate the ground deformation.

Fig. 10A compares the pressure profile of the poroelastic simulation and that of the property-changing model. At the end of year 5, the peak pressure is 1.3 percent smaller than the poroelastic value. Since the injector has a constant injection rate and right boundary is maintained at hydrostatic pressure (Fig. 3), if the permeability of the entire reservoir were twice larger the pore pressure would be halved according to Darcy's law. However, after five years only 5 percent of the reservoir has experienced permeability increase and as a result the pressure deviation observed in Fig. 10 A is

small. Fig. 10B compares the surface uplift of the poroelastic simulation and that of the property-changing model. At the end of year 5, the maximum surface uplift is 3.7 percent smaller than the poroelastic value, which results from smaller pore pressure and the compaction caused by the decrease in reservoir rock stiffness.

For longer injection, e.g., 50 years, the fraction of rock experiencing permeability change is much larger. If the boundary conditions are unchanged, i.e., CO_2 is injected at constant rate and water pressure is kept hydrostatically at the other end, the ground surface would subside significantly from its peak position. A better way to explore the permeability change is to have a constant downhole pressure at the injector, a slower water draining rate at the other end, or a higher CO_2 injection rate. In any case, the monitoring of CO_2 plume in carbonate reservoir via ground deformation becomes more complicated and better be combined with other measurements such as the wellhead monitoring.

6 Conclusions

We have preformed poroelastic simulation of CO_2 injection in Nisku carbonate formation in Alberta, Canada, and find 2.3 cm uplift after 5 years of injection. Based on three experimental studies [*Grgic*, 2011; *Le Guen et al.*, 2007; *Vialle and Vanorio*, 2011] on CO_2-water-carbonate interaction, we expect changes in rock stiffness and permeability along with the chemical dissolution of rock matrix. When CO_2 is injected into a low permeability formation at high rate, pore water is mostly flowing horizontally away from the injection well and vertical convection of water is limited in the short term. In this

case, the injected CO_2 being dry suggests there is limited water in dissolving the rock matrix, which is referred as the closed-system hypothesis. Based on this hypothesis and experimental data [*Vialle and Vanorio*, 2011], the rock stiffness is estimated to decrease by 2% and the permeability is estimated to be doubled. Accommodating the rock property change in the numeric simulation, we find the difference between the obtained ground deformation and that from the poroelastic behavior is limited after 5 years' injection. However, as a larger fraction of the reservoir rock experiences increase in permeability in the long term, the pore pressure would decrease when CO_2 injection rate is fixed and water is being pumped out in the other end. This brings complications in geodetic monitoring, and suggests usage of alternative injection scheme such as constant pressure at the injector. In this study, at least two important aspects are not considered and worth further study. One is the inelastic deformation associated with cracks and fractures, which inevitably exist in natural rocks. The other is the localization of rock dissolution due to either permeability heterogeneity or vertical convection induced by the dependence of water density on dissolved CO_2 in the long term.

References

Bachu, S., and B. Bennion (2008), Effects of in-situ conditions on relative permeability characteristics of CO2-brine systems, *Environmental Geology*, *54*(8), 1707-1722.

Batzle, M., and Z. Wang (1992), Seismic properties of pore fluids, *GEOPHYSICS*, *57*(11), 1396-1408.

Bennion, B., and S. Bachu (2010), Drainage and imbibition CO2/brine relative permeability curves at reservoir conditions for carbonate formations. SPE 134028

SPE Annual Technical Conference and Exhibition, Florence, Italy, paper presented at SPE Annual technical conference and exhibition, Florence, Italy, Society of Petroleum Engineers.

Benson, S., P. Cook, J. Anderson, S. Bachu, H. Nimir, B. Basu, J. Bradshaw, G. Deguchi, J. Gale, and G. von Goerne (2005), Underground geological storage, *IPCC special report on carbon dioxide capture and storage*, 195-276.

Clauser, C., and E. Huenges (1995), Thermal conductivity of rocks and minerals, *Rock physics and phase relations: a handbook of physical constants*, *3*, 105-126.

Coussy, O. (2004), *Poromechanics*, Wiley.

Duan, Z., and D. Li (2008), Coupled phase and aqueous species equilibrium of the H2O–CO2–NaCl–CaCO3 system from 0 to 250 °C, 1 to 1000 bar with NaCl concentrations up to saturation of halite, *Geochimica et Cosmochimica Acta*, *72*(20), 5128-5145.

Fenghour, A., W. A. Wakeham, and V. Vesovic (1998), The Viscosity of Carbon Dioxide, *Journal of Physical and Chemical Reference Data*, *27*(1), 31-44.

Ghaderi, S., and Y. Leonenko (2009), Reservoir modelling Wabamun Area CO2 Sequestration Project (WASP), *Energy and Environmental Systems Group Institute for Sustainable Energy, Environment and Economy (ISEEE), University of Calgary, Calgary, AB, Canada*.

Goodarzi, S., and A. Settari (2009), Geomechanical Modelling and Analysis Wabamun Area CO2 Sequestration Project (WASP), *Energy and Environmental Systems Group Institute for Sustainable Energy, Environment and Economy (ISEEE), University of Calgary, Calgary, AB, Canada*.

Grgic, D. (2011), Influence of CO2 on the long‐term chemomechanical behavior of an oolitic limestone, *Journal of Geophysical Research: Solid Earth (1978–2012)*, *116*(B7).

Hurter, S., D. Labregere, J. Berge, and A. Desitter (2008), Impact of mutual solubility of H2O and CO2 on injection operations for geological storage of CO2.

Lavoie, R., and D. Keith (2010), Executive Summary Wabamun Area CO2 Sequestration Project (WASP), *Energy and Environmental Systems Group Institute for Sustainable Energy, Environment and Economy (ISEEE), University of Calgary, Calgary, AB, Canada*.

Le Guen, Y., F. Renard, R. Hellmann, E. Brosse, M. Collombet, D. Tisserand, and J.-P. Gratier (2007), Enhanced deformation of limestone and sandstone in the presence of high PCO2 fluids, *Journal of geophysical research*, *112*(B5), B05421.

Lu, C., W. S. Han, S.-Y. Lee, B. J. McPherson, and P. C. Lichtner (2009), Effects of density and mutual solubility of a –brine system on storage in geological formations: "Warm" vs. "cold" formations, *Advances in Water Resources*, *32*(12), 1685-1702.

Mathieson, A., J. Midgley, K. Dodds, I. Wright, P. Ringrose, and N. Saoul (2010), CO2 sequestration monitoring and verification technologies applied at Krechba, Algeria, *The Leading Edge*, *29*(2), 216-222.

Mogi, K. (1958), Relations between the eruptions of various volcanoes and the deformations of the ground surfaces around them.

Morris, J. P., Y. Hao, W. Foxall, and W. McNab (2011), A study of injection-induced mechanical deformation at the In Salah CO2 storage project, *International Journal of Greenhouse Gas Control*, *5*(2), 270-280.

Nordbotten, J. M., and M. A. Celia (2006), Similarity solutions for fluid injection into confined aquifers, *Journal of Fluid Mechanics*, *561*, 307-327.

Nygaard, R. (2010), Geomechanical Analysis Wabamun Area CO2 Sequestration Project (WASP), *Energy and Environmental Systems Group Institute for Sustainable Energy, Environment and Economy (ISEEE), University of Calgary, Calgary, AB, Canada*.

Okada, Y. (1985), Surface deformation due to shear and tensile faults in a half-space, *Bulletin of the seismological society of America*, *75*(4), 1135-1154.

Peters, G. P., G. Marland, C. Le Quéré, T. Boden, J. G. Canadell, and M. R. Raupach (2011), Rapid growth in CO2 emissions after the 2008-2009 global financial crisis, *Nature Climate Change*, *2*(1), 2-4.

Preisig, M., and J. H. Prévost (2011), Coupled multi-phase thermo-poromechanical effects. Case study: CO2 injection at In Salah, Algeria, *International Journal of Greenhouse Gas Control*, *5*(4), 1055-1064.

Riaz, A., M. Hesse, H. Tchelepi, and F. Orr (2006), Onset of convection in a gravitationally unstable diffusive boundary layer in porous media, *Journal of Fluid Mechanics*, *548*(1), 87-111.

Robertson, E. C. (1988), *Thermal properties of rocks*, US Department of the Interior, Geological Survey.

Rutqvist, J., D. W. Vasco, and L. Myer (2010), Coupled reservoir-geomechanical analysis of CO2 injection and ground deformations at In Salah, Algeria, *International Journal of Greenhouse Gas Control*, *4*(2), 225-230.

Scalabrin, G., P. Marchi, F. Finezzo, and R. Span (2006), A Reference Multiparameter Thermal Conductivity Equation for Carbon Dioxide with an Optimized Functional Form, *Journal of Physical and Chemical Reference Data*, *35*(4), 1549-1575.

Sengers, J. V., J. T. R. Watson, R. S. Basu, B. Kamgar-Parsi, and R. C. Hendricks (1984), Representative Equations for the Thermal Conductivity of Water Substance, *Journal of Physical and Chemical Reference Data*, *13*(3), 893-933.

Span, R., and W. Wagner (1996), A New Equation of State for Carbon Dioxide Covering the Fluid Region from the Triple-Point Temperature to 1100 K at Pressures up to 800 MPa, *Journal Name: Journal of Physical and Chemical Reference Data; Journal Volume: 25; Journal Issue: 6; Other Information: PBD: Nov 1996*, Medium: X; Size: pp. 1509-1596.

Sun, H., R. Feistel, M. Koch, and A. Markoe (2008), New equations for density, entropy, heat capacity, and potential temperature of a saline thermal fluid, *Deep Sea Research Part I: Oceanographic Research Papers*, *55*(10), 1304-1310.

Vasco, D., A. Rucci, A. Ferretti, F. Novali, R. Bissell, P. Ringrose, A. Mathieson, and I. Wright (2010), Satellite ‐ based measurements of surface deformation reveal fluid flow associated with the geological storage of carbon dioxide, *Geophysical Research Letters*, *37*(3).

Vialle, S., and T. Vanorio (2011), Laboratory measurements of elastic properties of carbonate rocks during injection of reactive CO2-saturated water, *Geophysical Research Letters*, *38*(1), L01302.

Waples, D. W., and J. S. Waples (2004), A review and evaluation of specific heat capacities of rocks, minerals, and subsurface fluids. Part 2: fluids and porous rocks, *Natural resources research*, *13*(2), 123-130.

Table 1

Mechanical, transportation and thermal properties of the reservoir, overburden and underburden.

Layer number*	E (GPa)	ν	N (GPa)	b	ϕ	k (mD)	kr_{BRINE}	kr_{CO2}	Pc (MPa)	T_0 (°C)	C (kJ/kg/K)	K_T[£] (W/m/K)	α (1/K)
1	8.5	0.32	-	-	-	-	-	-	-	-	-	-	-
2	13.3	0.29	-	-	-	-	-	-	-	-	-	-	-
3	27.4	0.28	-	-	-	-	-	-	-	-	-	-	-
4	24.8	0.27	91	0.70	0.04	2.9×10^{-6}	-	-	-		0.77	$0.7+770/(T+77)$	2.7×10^{-5}
5	28.9	0.29	123	0.71	0.1	45.92	$0.26S_w$[¶]	$(1-S_w)^5$	$(1-S_w)$[$]	60-28y	1	$0.7+770/(T+77)$	2.4×10^{-5}
6[†]	24.8	0.27	91	0.70	0.04	2.9×10^{-6}	-	-	-		0.77	$0.7+770/(T+77)$	2.7×10^{-5}
7	24.8	0.27	-	-	-	-	-	-	-	-	-	-	-
8	75	0.25	-	-	-	-	-	-	-	-	-	-	-

* See Fig. 5 for the numbering of the layers. From left to right, the properties are Young's modulus, Poisson's ratio, Biot's tangent modulus, Biot's coefficient, porosity, absolute permeability, relative permeability of brine, relative permeability of CO_2 phase, initial temperature, specific heat of rock, thermal conductivity of rock, and volumetric thermal expansion coefficient. In the content of the table, T is the temperature in kelvin, S_w is the water saturation, and y is the vertical distance away from the bottom of the reservoir in km.

[†] Due to lack of data, property of layer 4 is used in place of those of layer 6 and 7.

[£] The thermal conductivity of rock is used as the average thermal conductivity in Eq. 11 as both the porosity and the permeability are small.

[¶] Bennion and Bachu (2010) report their relative permeability in Corey model, and shown is a smoother refit of the highest relative permeability in their test on the Nisku samples.

[$] The simulation was done by finite element method, and the arbitrary and somewhat large capillary pressure is used to keep numerical stability

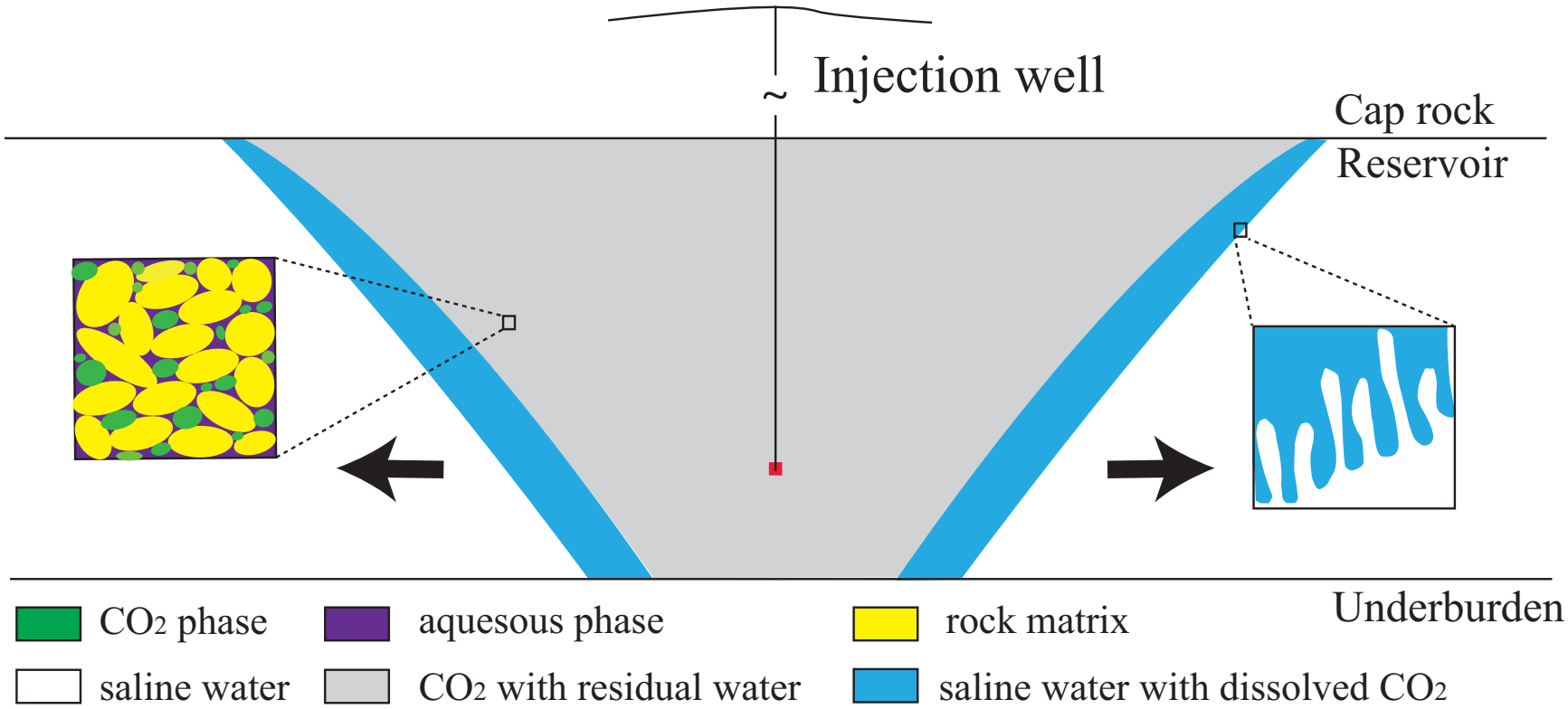

Figure 1. A schematic plot of the CO_2 injection in saline aquifer. In the gray region, a separate CO_2 phase coexists with the residual aqueous phase. In the blue region, the CO_2 is completely dissolved in the aqueous phase. The sizes of the gray and blue regions increase as the injection progresses. The zoomed-in box on the left shows the trapped wetting phase in the two-phase zone. The zoomed-in box on the right shows the gravity-driven fingering, of which the critical time and critical wavelength depends strongly on the permeability of the reservoir. The shape of the CO_2 plume shown in this figure is typical when CO_2 is injected into a low permeability formation at a high injection rate in the short term, and the arrows show the dominant directions of water migration in such a case.

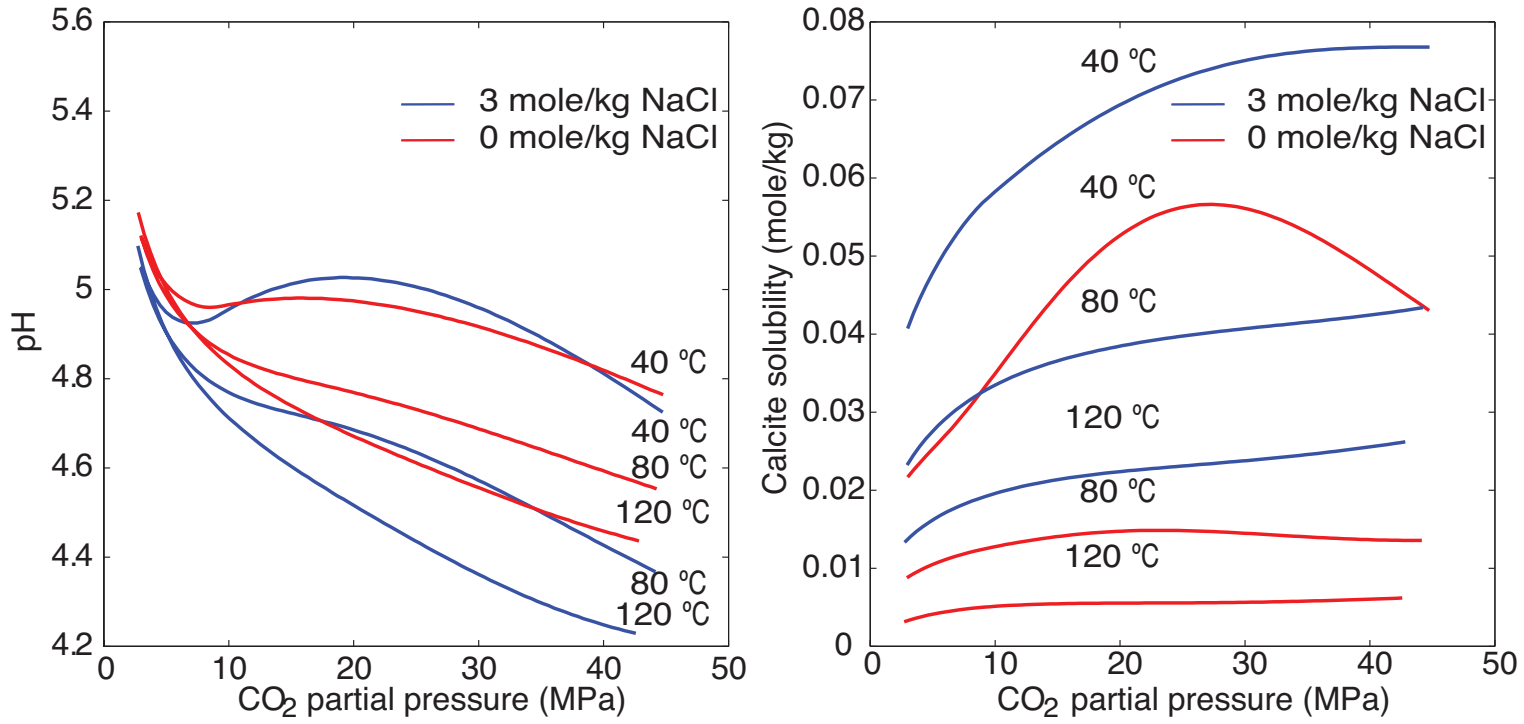

Figure 2. The pH and calcite solubility of brine as functions of CO_2 partial pressure under different temperatures and salinities calculated from the program from Duan and Li (2008).

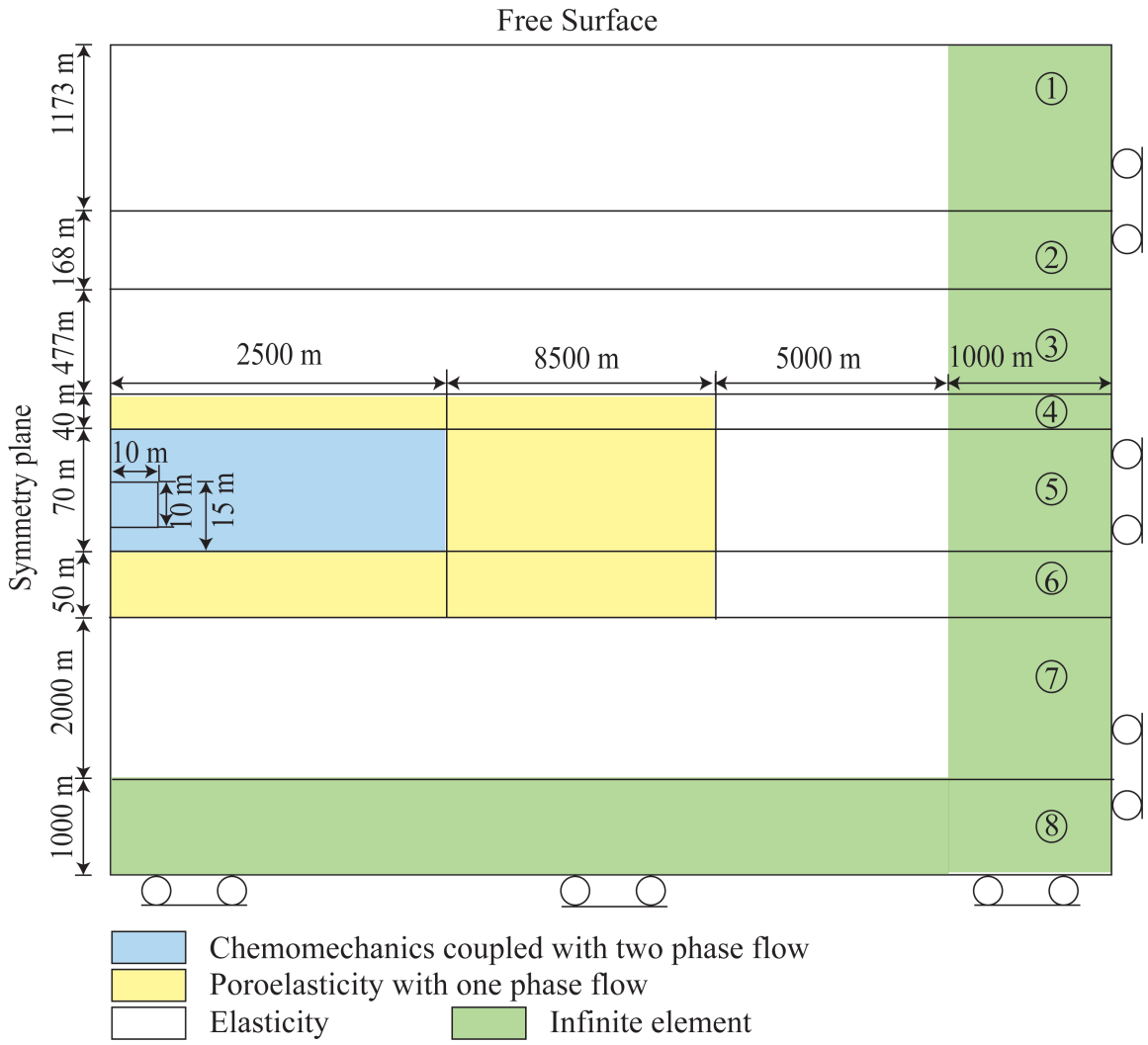

Figure 3. Model geometry for the coupled simulation of CO_2 flow and rock deformation. Material property of each layer can be found in Table 1. CO_2 is injected via the left side of the 10 m by 10 m square inside the blue subdomain at a rate of 0.2 Mt/km. Temperature evolution is calculated in the first 2.5 km from the left in layer 4-6. CO_2 flow is calculated in the blue domain. Brine flow is calculated in both the blue and yellow subdomains. Geomechanics calculations are preformed in the entire domain.

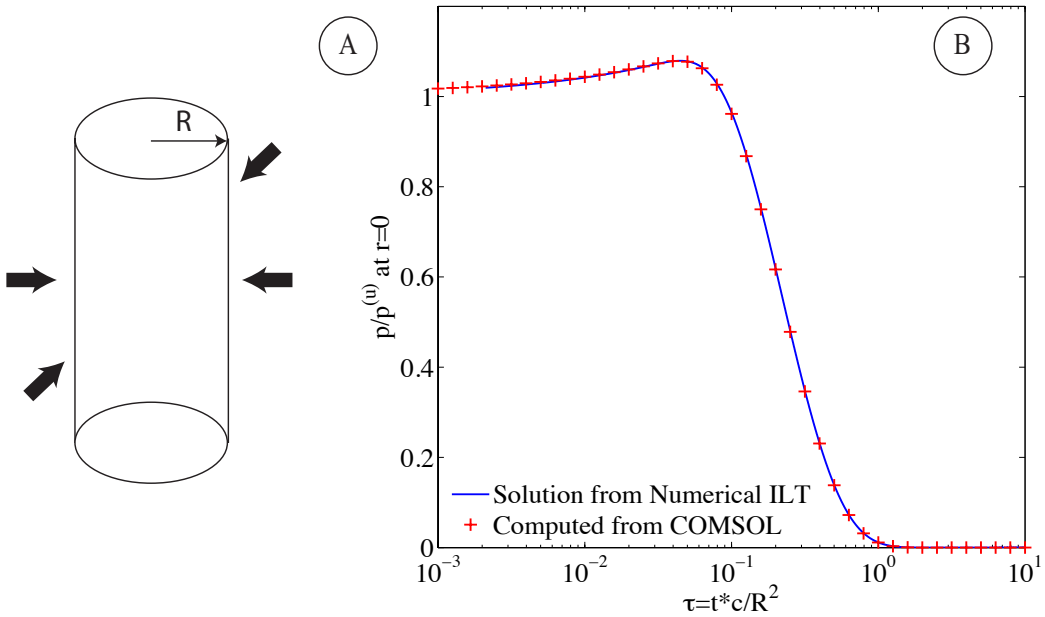

Figure 4. (A) Sudden pressurization of an infinitely long cylinder. (B) Plot of non-dimensional pressure at the center against non-dimensional time. The blue curve is calculated from numerical inverse Laplace transformation of the analytical solution in the frequency domain, and the red plus signs are calculated from finite element simulation.

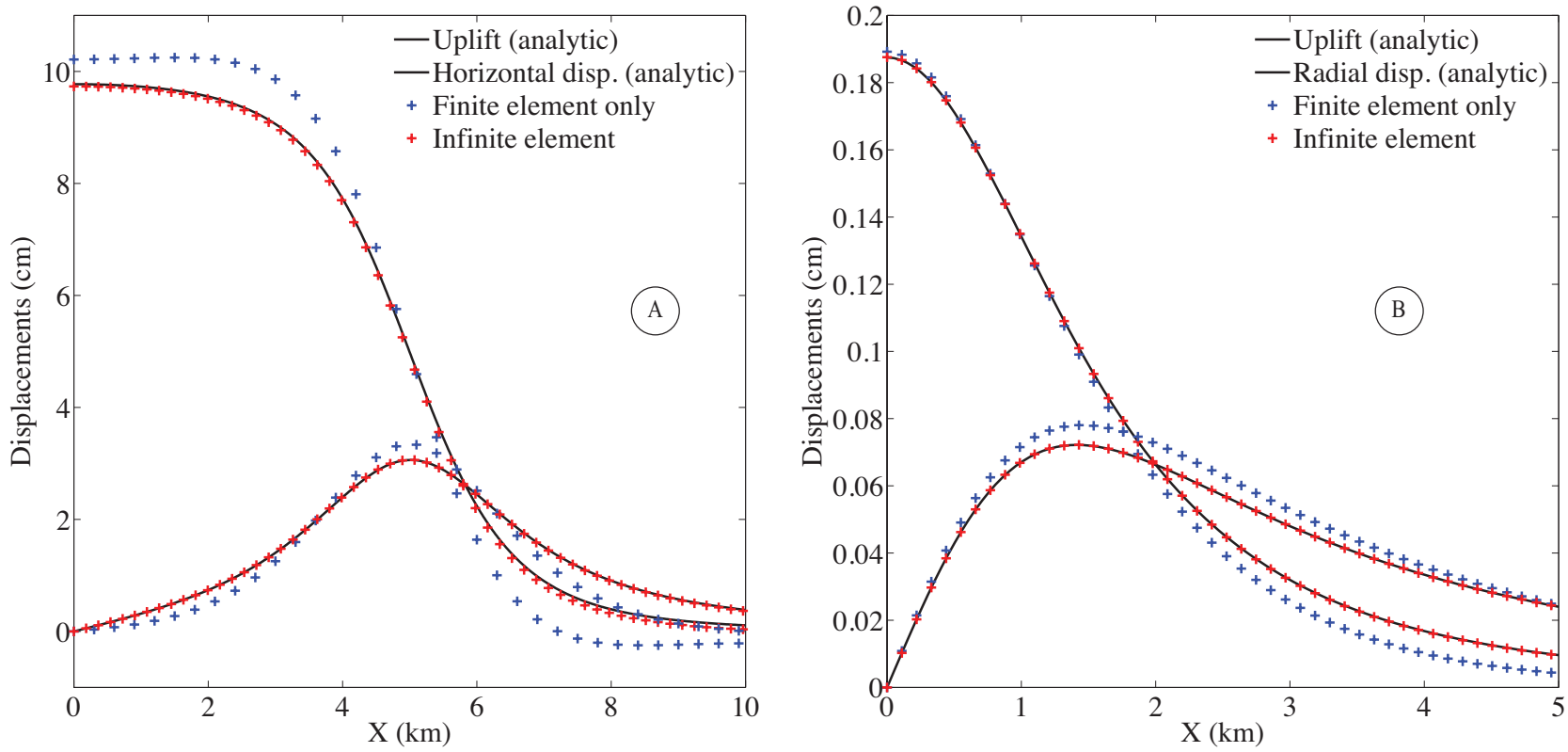

Figure 5. Comparison of ground deformation obtained from analytical solution, finite element only calculation, and infinite element and finite element coupled calculation for two models. The opening up of a 10 km wide and infinite long zero-dip rectangular crack causes the surface uplift on the left. The pressurization (10 MPa) of a spherical cavity with a radius of 200 m at a depth of 2 km causes the surface uplift on the right.

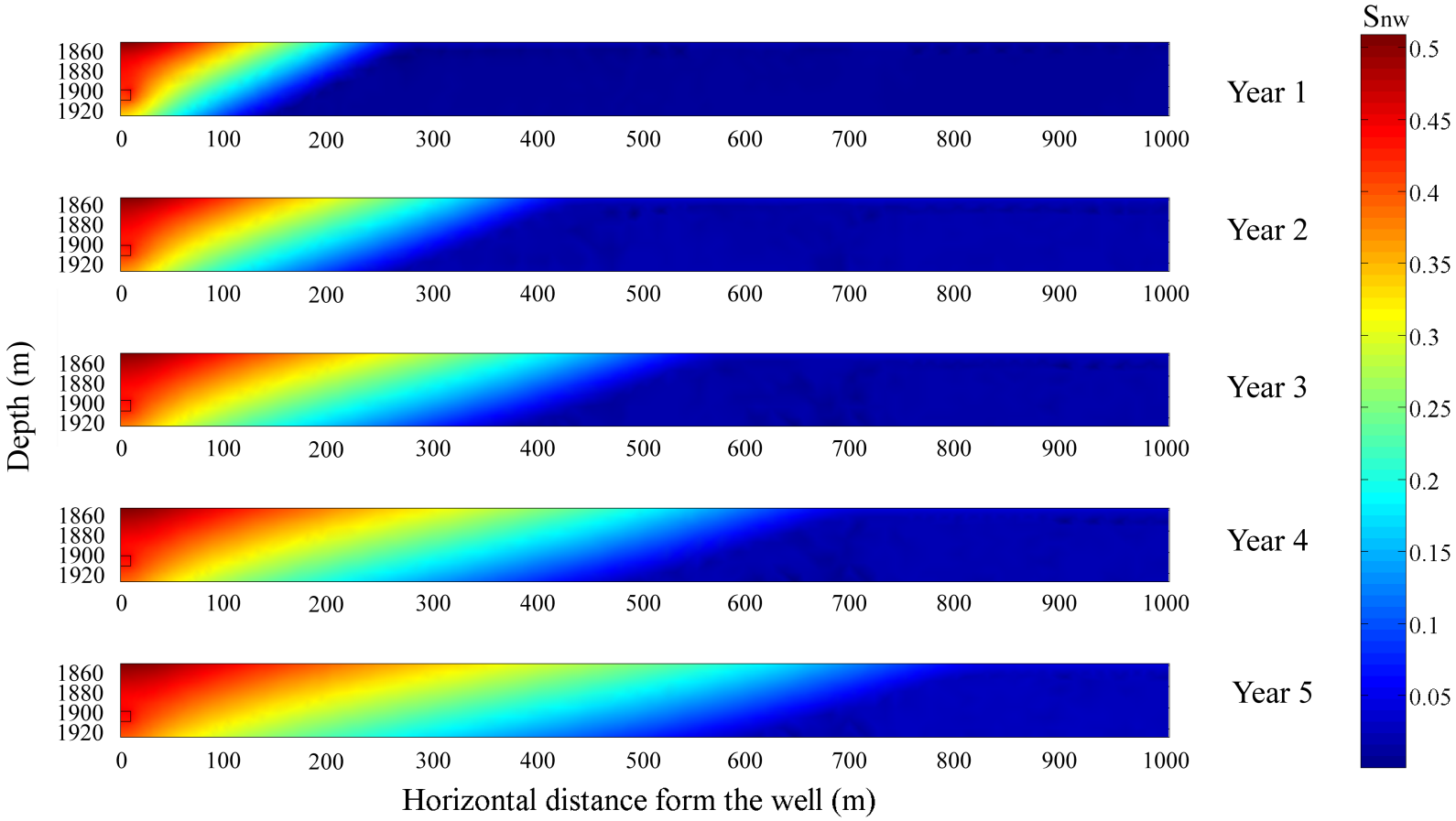

Figure 6. Propagation of the CO_2 plume in the reservoir.

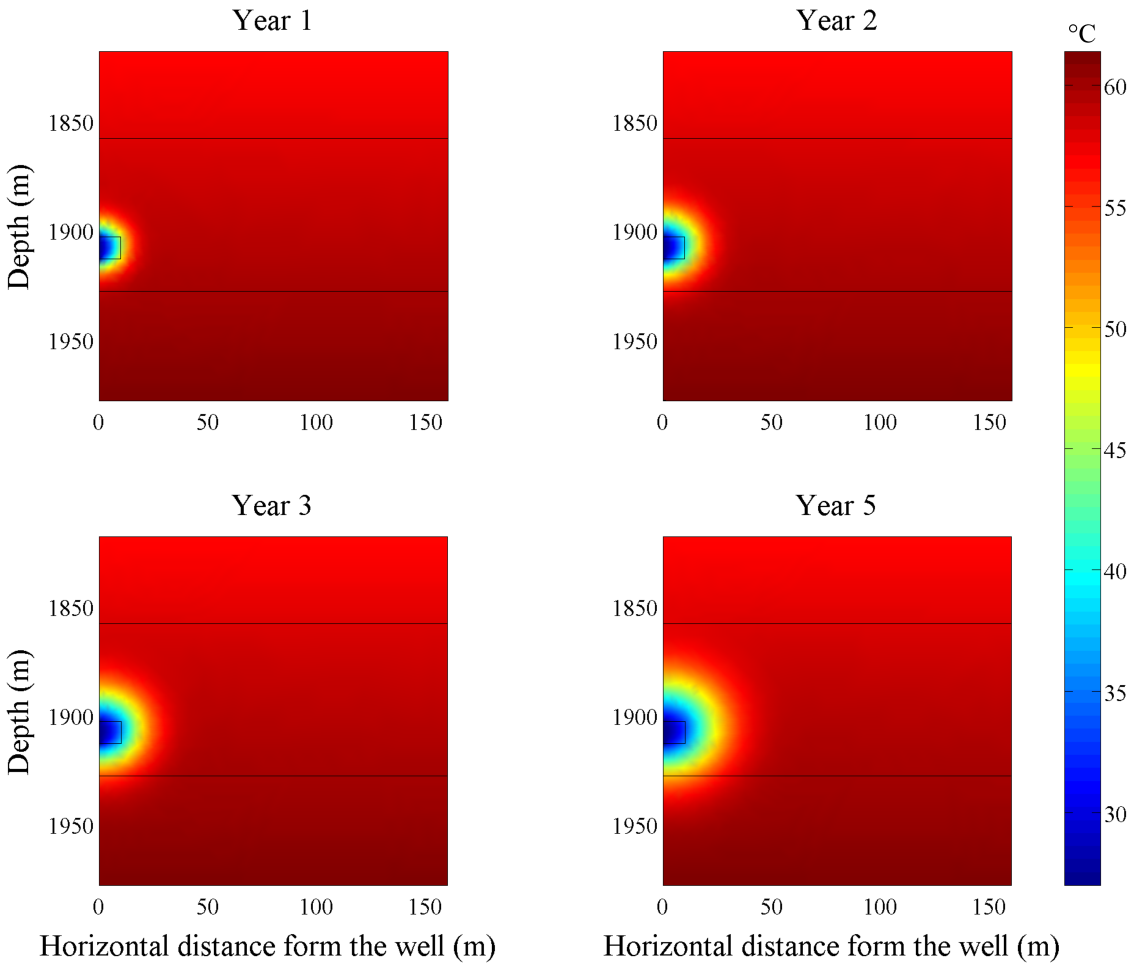

Figure 7. Evolution of the temperature in the reservoir and its immediate overburden and underburden.

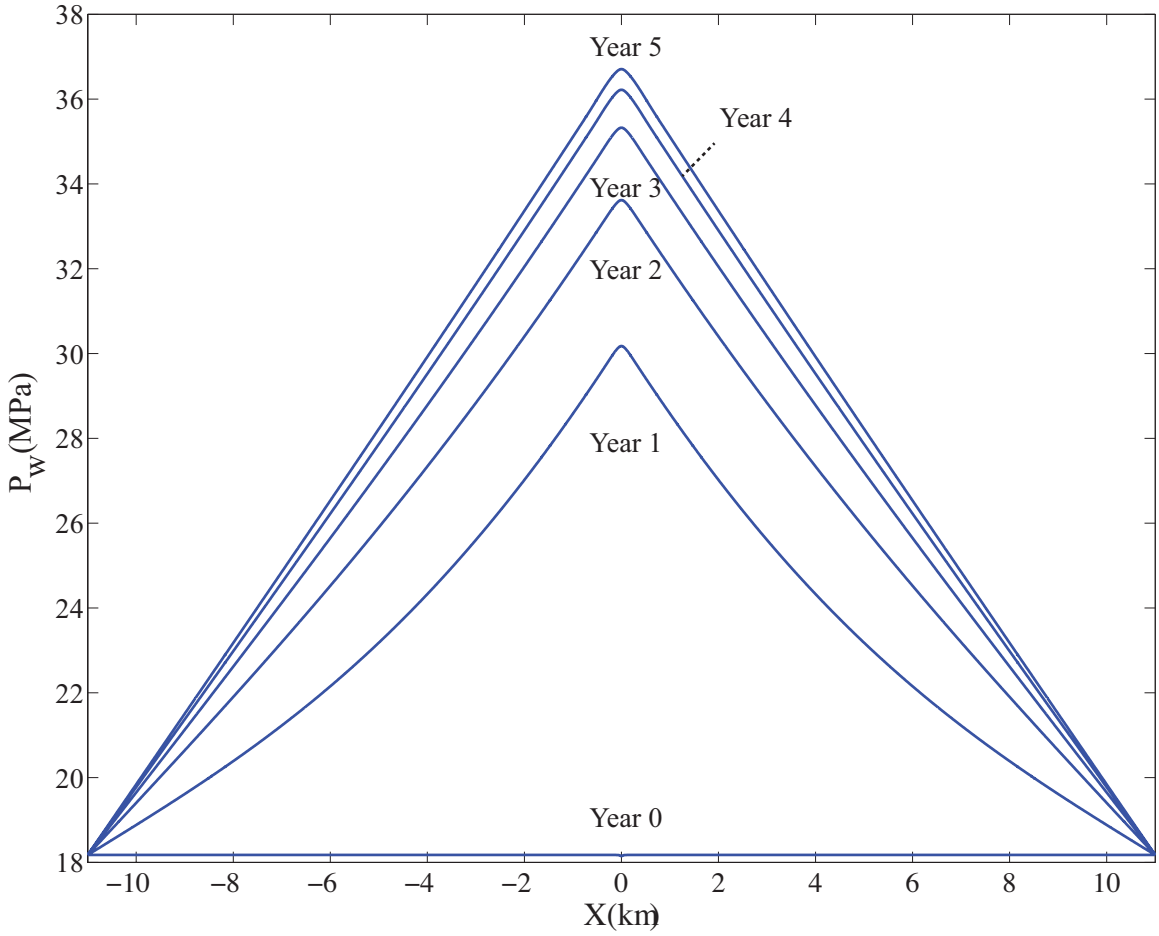

Figure 8. Evolution of the water pressure in the middle plane of the reservoir with time.

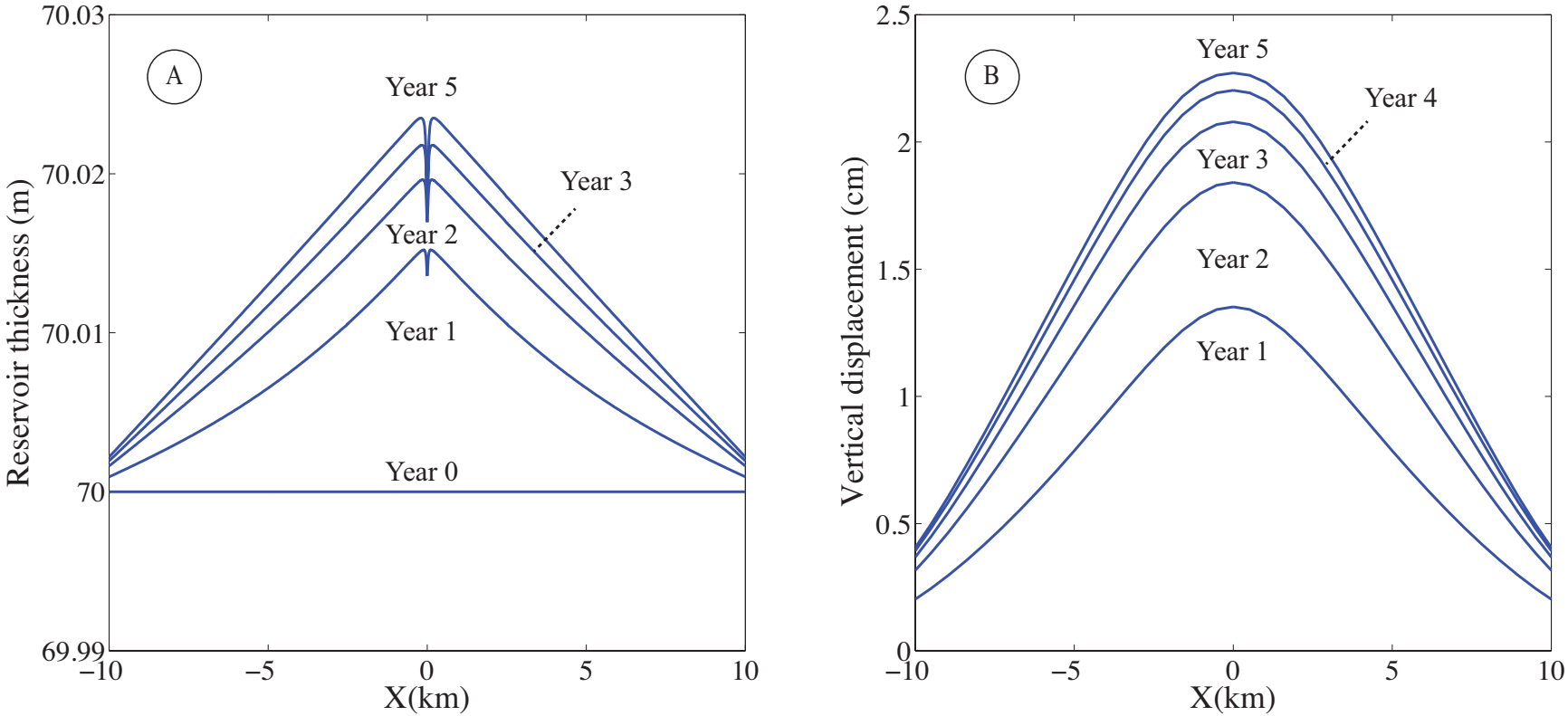

Figure 9. (A) The thickness of the inflated reservoir evolves with time. (B) The ground uplift evolves with time.

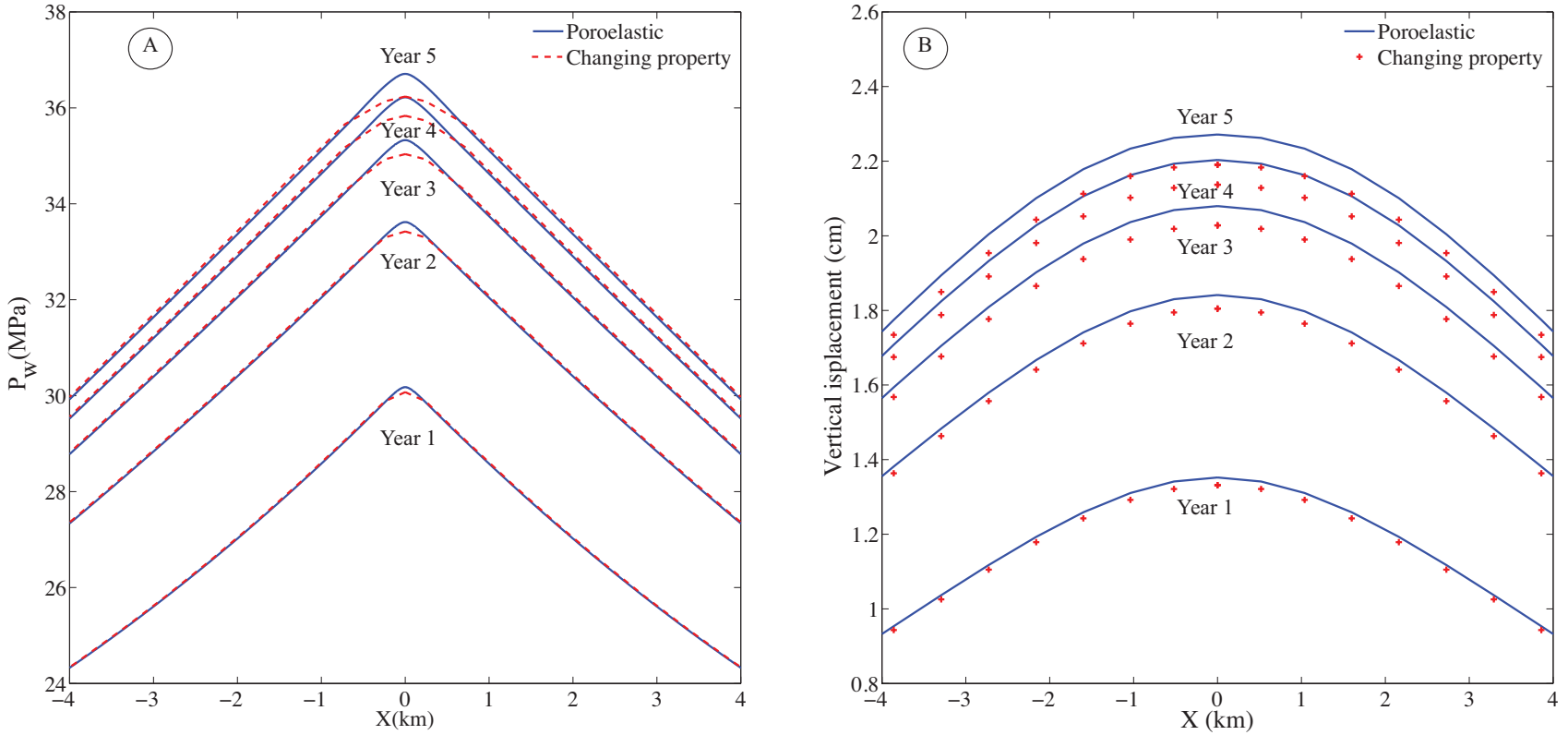

Figure 10. Pressure profile and surface deformation calculated from poroelastic constitutive law and the chemo-mechanical interaction described in section 5.